

# Excited state photoelectron spectroscopy of anisole†

C. G. Eisenhardt,<sup>a</sup> A. S. Gemechu,<sup>a</sup> H. Baumgärtel,<sup>\*a</sup> R. Chelli,<sup>bc</sup> G. Cardini<sup>bc</sup> and S. Califano<sup>bc</sup>

<sup>a</sup> Institut für Chemie—Physikalische und Theoretische Chemie, Freie Universität Berlin, Takustr. 3, 14195 Berlin, Germany

<sup>b</sup> Dipartimento di Chimica, University of Florence, via G. Capponi 9, 50121 Florence, Italy

<sup>c</sup> LENS, Largo E. Fermi 2, 50125 Florence, Italy

Received 11th June 2001, Accepted 16th August 2001

First published as an Advance Article on the web 17th October 2001

Excited state photoelectron spectra of anisole have been measured using different excitation pathways. They have been chosen according to vibrational levels in the  $S_1$  state as observed in the REMPI spectrum. The combination of extended *ab initio* calculations with the spectroscopic results leads to the frequencies and assignment of the 42 normal modes of the anisole cation and neutral anisole. A strong influence of the excitation pathway on the appearance of the photoelectron spectra has been observed. With increasing excitation energies the dominant signals in the spectrum are shifted to higher energy. The analysis of the spectra reveals that the major contribution to the intensity is caused by the population of vibrational combination states in the ion. Increasing the energy of the intermediate  $S_1$  state changes the population of these final states selectively. In addition, the population of the  $\nu_{9b}$  state is strongly supported by changes of the geometry in the  $S_1$  intermediate state.

## 1. Introduction

The understanding of the structure and electronic properties of van der Waals complexes between benzene derivatives and small molecules has witnessed in the last few years a considerable success thanks to the synergetic combination of molecular beam experiments coupled to different laser spectroscopic techniques and *ab initio* quantum mechanical calculations.

Different research groups have studied in detail aggregates containing small molecules associated to a phenol molecule or to its cation.<sup>1–21</sup> Hydrogen bonding plays a very important role in the structure of these complexes in which phenol acts as proton donor to small molecules like water, ammonia, *etc.* acting as proton acceptors. Recent *ab initio* calculations have actually shown that structures in which the H-bonded molecule lies in the same plane as the aromatic ring are energetically favored with respect to structures in which it lies above the benzene ring, as found in complexes of benzene with  $N_2$ , CO, CS<sub>2</sub> and rare gases.

Very little however is known about complexes in which the aromatic molecule acts as a proton acceptor<sup>22</sup> and even less about their cationic species. In particular, if the O–H group of phenol is blocked by substitution of the hydrogen atom with an aliphatic group, the possibility of hydrogen bond coupling to an acceptor molecule is lost and the question arises whether the complex formation is dominated by the interaction with the  $\pi$  electron system, as occurs in the benzene complexes, or by the interaction with the phenyl C–H bonds.

In order to understand the structure and the dynamics of such aggregates we have studied (by REMPI and photoelectron spectroscopy) anisole and the corresponding cations, implementing the structure determination by *ab initio* quantum mechanical calculations.

The interpretation of the spectra of the complexes is rather difficult and requires as a preliminary step a correct understanding of the spectra of the parent molecules. For this reason, in the present paper we report on the interpretation of the REMPI and photoelectron spectra of anisole and of the anisole cation, with particular emphasis on the importance of different ionization pathways. In forthcoming papers we shall discuss the structure and spectra of their complexes with a series of small molecules, including CO<sub>2</sub>, NH<sub>3</sub> and N<sub>2</sub>O.

The vibrational spectrum of anisole in the electronic groundstate has been reported and discussed by several authors, but finally it was Balfour<sup>23</sup> who gave a complete and convincing assignment of the normal modes based on the IR-spectra of anisole and different specific deuterated anisoles. His assignment fits well to the energies and characters of these modes as obtained by quantum chemical calculations performed in this work.

In the past *ab initio* calculations were made using the HF-level with STO-3G basis set.<sup>24</sup> Recently Rumi and Zerbi<sup>25</sup> used the HF-level of the theory with the 3-21G and 6-31G\*\* basis set to investigate the pi-electron conjugation and back donation effect on the infrared activity of the CH<sub>3</sub> stretching vibrations. Using the 3-21G basis set they also calculated the dependence of the vibrational pattern (Raman and IR) and the first and second hyperpolarizability from the torsional angle around the aryl carbon–oxygen bond. Comparable high level calculations have been published recently by Tsuzuki *et al.*<sup>26</sup> They investigated the influence of intramolecular hydrogen bonding in *o*-hydroxyanisole on the torsional barrier of the O–CH<sub>3</sub> group. To our knowledge no calculations on the anisole cation are yet available. It should be mentioned that quantum chemical calculations based on the density functional theory or HF methods in the present state work well only for the electronic ground state. Calculation of the first excited state with sufficient accuracy is not possible at the moment with commonly available programs. Therefore the assignment

† Dedicated to Professor F. Dörr on the occasion of his 80th birthday.

of vibrations in the  $S_1$  state is based on comparing their frequencies with those in the electronic ground state. The geometry of anisole in the  $S_1$  state has been obtained from the analysis of the rotational structure in the highly resolved  $S_1-S_0$  (0,0) transition.<sup>27</sup>

The He(I) photoelectron spectrum of anisole has been reported in the literature.<sup>28</sup> It reveals clearly the sequence of electronic states up to 21.2 eV but due to the limited energy resolution and signal to noise ratio in the early days of photoelectron spectroscopy vibrational spacing is hardly recognized.

Excited state photoelectron spectroscopy in its simplest form is performed by using a single laser tuned so as to give rise to a specific excited vibronic state. Absorption of a second photon then produces the ion, if the total energy of the two absorbed photons exceeds the first ionization potential of the molecule. Using low laser power, the ionization is a sequential process. To obtain appropriate resonant intermediate states the measurement of the REMPI spectrum prior to the excited state photoelectron spectroscopy is unavoidable.

The combination of excited state photoelectron spectroscopy with the molecular beam technique improves the energy resolution and the signal to noise ratio considerably in comparison to conventional He(I) photoelectron spectroscopy. It opens the possibility to observe the vibrational states in larger cations directly or indirectly *via* overtones and combinations.

## 2. Experimental

Fig. 1 shows a schematic drawing of the experimental set-up. It consists of a supersonic beam (expansion chamber) coupled to a time of flight spectrometer, a tunable dye laser and a data acquisition system. The set-up has briefly been described in previous works.<sup>29,30</sup> In the following some important details of the instrument will be outlined.

The photoelectron spectrometer ("magnetic bottle" type<sup>31,32</sup>) is made up of a  $\text{Sm}_2\text{Co}_{17}$  permanent magnet, an adjustable solenoid magnet, a drift tube and a detector. The photoionization occurs 4 mm above the permanent magnet. In the ionization region the magnetic field has a value of about 0.1 T. In the magnetic field the electrons are tightly constrained to follow the local field lines. The weak field (0.25 mT) of the long coaxial solenoid magnet directs the produced photoelectrons through a small aperture down the full length (100 cm) of the time-of-flight tube. The flight tube is shielded from stray magnetic fields by a layer of " $\mu$ "-metal (Vacuumschmelze). At the end of the tube the electrons are accelerated towards a double microchannel plate detector. By using two additional electrodes (*cf.* Fig. 1) the photoelectron spectrometer can be operated as a two-step TOF mass spectrometer<sup>33</sup> for REMPI spectroscopy. The third aperture

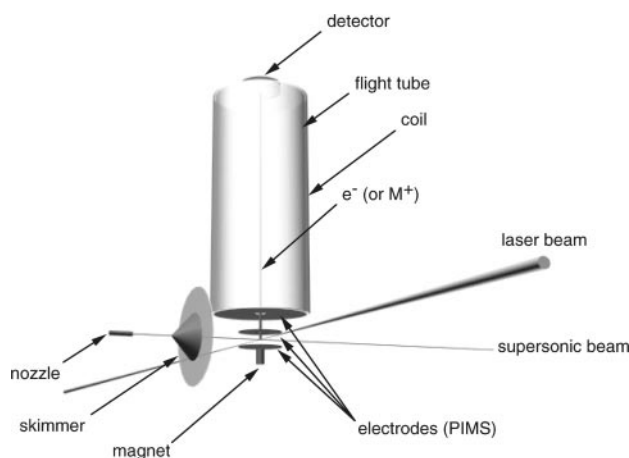


Fig. 1 The essential parts of the experimental set-up.

of the mass spectrometer acts as the flight tube entrance. The main vacuum chamber and the tube are manufactured of aluminium to avoid magnetic influence. The surfaces are coated with copper to minimize surface charging and to improve the vacuum efficiency. All parts of the spectrometer are carefully grounded.

The detector output is coupled to a fast transimpedance amplifier *via* a high-voltage capacitor.<sup>34</sup> The signals are recorded with 1 ns resolution on a digital storage oscilloscope (Le Croy 9370) and read out *via* a GPIB interface by a computer.

We used a 50  $\mu\text{m}$  nozzle and a 300  $\mu\text{m}$  skimmer to admit the molecules from the molecular beam source to the ionization chamber. Ionization is achieved by the frequency-doubled output of a Nd-YAG (10 Hz repetition rate) pumped dye laser (Estla Ltd. DL-MIDI), calibrated with a neon OG lamp. Coumarin 153 dissolved in methanol is used as dye. The resolution of the REMPI spectra is limited by the spectral laser width to 0.25  $\text{cm}^{-1}$ . The energy resolution of the photoelectron spectrometer depends strongly on the electron kinetic energy. The 1 ns sampling rate of the oscilloscope corresponds, for example, to an energy resolution of 0.34 meV for electrons of 0.44 eV kinetic energy and to 3.9 meV for electrons of 2.2 eV kinetic energy. Since the spectrometer collects almost every emitted photoelectron, the halfwidth of the signal depends mainly on the "turning time" of those electrons which start moving in the direction opposite to that of the detector. This time is also a function of the electron energy. For an electron kinetic energy of 0.44 eV the FWHM of the resulting signal is equal to 18 meV. The energy scale has been calibrated using Kimura's value of  $8.2320 \pm 0.0004$  eV<sup>35</sup> for the adiabatic ionization potential of anisole. The onset of our electron yield refers to this energy. In the literature<sup>28</sup> a value of  $8.21 \pm 0.02$  eV based on He(I) spectra has been reported. With our calibration procedure we are able to measure the energies of all other states with an absolute accuracy of 5 meV.

Each PES is an average of 5000 time of flight spectra. The signal to noise ratio is excellent; even at a photoelectron energy of 0.2 eV it exceeds a value of five.

## 3. Results and discussion

### 3.1. *Ab initio* calculations

The calculations were carried out by the density functional theory<sup>36</sup> (DFT) as implemented in the GAUSSIAN 98 package.<sup>37</sup> In DFT good results are achieved by using a smaller basis set than required in other correlated methods. However, it is important to choose an appropriate combination of basis set and exchange-correlation functionals, as shown by Rauhut and Pulay<sup>38</sup> and by Scott and Radom.<sup>39</sup> The combination of the 6-31G(d) basis set<sup>40</sup> with the B3-LYP exchange-correlation functional represents a good compromise between accuracy and computer time cost. Of course, the agreement of the calculation with experimental data can be improved using a larger basis set. Therefore we used the B3-LYP functional and the 6-311G++(d,p) basis set.

The B3-LYP functional is defined in terms of the Dirac-Slater (DS), Hartree-Fock (HF), Becke (B88),<sup>41</sup> Lee-Yang-Parr (LYP)<sup>42</sup> and Vosko-Wilk-Nusair (VWN)<sup>43</sup> functionals according to the expression:

$$F_{\text{B3-LYP}} = 0.8F_{\text{x}}(\text{DS}) + 0.2F_{\text{x}}(\text{HF}) + 0.72F_{\text{x}}(\text{B88}) + 0.81F_{\text{c}}(\text{LYP}) + 0.19F_{\text{c}}(\text{VWN}) \quad (1)$$

The minimum energy geometry of both anisole and anisole cation were obtained using "very tight" convergence criteria. The maximum force on the atoms and the root mean square of the forces were less than  $10^{-6}$  a.u. The same criterion ( $10^{-6}$  a.u.) was used for the maximum atomic displacement (between

consecutive self-consistent iterations) and the root mean square of the atomic displacements. During the calculation of the second derivatives with respect to the atomic displacements, a very fine grid<sup>37</sup> was adopted for the numerical computation of the integrals to increase the accuracy. In the literature several scaling frequency factors are normally<sup>38</sup> used for different types of internal coordinates. We have found that a satisfactory fit of the experimental frequencies is obtained by scaling the calculated frequencies in the range up to 2000  $\text{cm}^{-1}$  by the factor 0.973 and those in the higher frequency range by the factor 0.963.

The calculated bond lengths and angles for neutral anisole and for the anisole cation are shown in Fig. 2. Comparison of the two structures shows some significant differences. In the cation the C–O–CH<sub>3</sub> angle increases by more than 4° with respect to the neutral molecule. In addition the length of the two C–C bonds adjacent to the C–O bond increases by about 0.04 Å from anisole to the anisole cation, whereas that of the two next C–C bonds decreases by about 0.03–0.02 Å. The other two C–C bonds increase, both by more than 0.02 Å. These features show the increase of quinoidal character for the anisole cation as found for the first excited state from the rotational structure of the  $S_1 \leftarrow S_0$  transition.<sup>27</sup>

The calculated *ab initio* normal mode frequencies of neutral anisole and of the anisole cation are compared to the experimental frequencies in Table 1.

The calculated frequencies agree very well with the experimental ones, differences being on average of the order of few wavenumbers. The assignment of the normal modes of anisole has been previously discussed by Owen and Hester<sup>44</sup> and, more recently, by Balfour.<sup>23</sup> Our assignment, based on the comparison with the *ab initio* calculations, agrees well with

Balfour's assignment. The only difference concerns the CH<sub>3</sub> symmetric stretching mode. The frequency of this mode, assigned by Balfour to a band at 2834  $\text{cm}^{-1}$ , is too low with respect to known CH<sub>3</sub> stretching frequencies of methoxy groups in substituted benzene compounds. For this reason, Owen and Hester<sup>44</sup> discussed the possibility that the occurrence of this band is due to a Fermi resonance between the CH<sub>3</sub> symmetric stretching mode and the overtone of the symmetric bending CH<sub>3</sub> mode at 1442  $\text{cm}^{-1}$  and suggested as an alternative assignment for the stretching mode a band in the 2950  $\text{cm}^{-1}$  region. Recently, Rumi and Zerbi<sup>25</sup> have presented strong evidence against the assignment of the band at 2834  $\text{cm}^{-1}$  to a fundamental mode. Our calculation shows that there is no calculated frequency in the 2850  $\text{cm}^{-1}$  region and therefore we assign the asymmetric CH<sub>3</sub> stretching mode to the band at 2942  $\text{cm}^{-1}$  as proposed in ref. 44.

Since in anisole the O–CH<sub>3</sub> group can undergo a large scale rotation about the C–O bond, its molecular symmetry should in principle be classified according to Longuet-Higgins theory as belonging to the  $G_4$  group. The  $G_4$  group is isomorphous with the  $C_{2v}$  group and has the same character table. This presents no difficulty for the classification of the skeleton modes but requires a different classification of the rotational modes. Since, however, in previous papers the skeleton modes were classified according to the symmetry species  $A_1$ ,  $A_2$ ,  $B_1$  and  $B_2$  of the  $C_{2v}$  group and those of the methoxy group according to the symmetry species  $a'$  and  $a''$  of the  $C_s$  group, for an easier comparison with the literature, we shall adopt this second classification. For the vibrations of the aromatic ring we adopt the well-known notation of Wilson.<sup>46</sup>

For the anisole cation the frequencies of the normal modes are not available in the literature. The experimental frequencies listed in Table 1 up to about 1100  $\text{cm}^{-1}$  are taken from an unpublished ZEKE spectrum measured by Kimura.<sup>35</sup> The other frequencies were assigned from an analysis of the fine structure of the  $0 \leftarrow 0$  photoelectron spectrum discussed in section 3.3.1, using as a guide the calculated frequencies. The procedure allowed us not only to identify with high accuracy the normal modes, but also a large number of binary and ternary combinations in the spectrum and this makes us confident in the reliability of the proposed assignment.

### 3.2. The REMPI spectrum

In order to understand the features of the photoelectron spectra it is meaningful to assign the resonant intermediate vibrational states used in the photoionization process. The measurement of a REMPI spectrum is a necessary step in identifying the energy of the resonant intermediate states used in the different excited state photoelectron spectra.

The anisole REMPI spectrum shown in Fig. 3 has been measured in the range 276–267 nm (36 232–37 453  $\text{cm}^{-1}$ ), i.e. in a range extending for about 1200  $\text{cm}^{-1}$  above the origin of the  $S_1 \leftarrow S_0$  transition at 36 382  $\text{cm}^{-1}$ , in reasonable agreement with the value of 36 386  $\text{cm}^{-1}$  reported in the literature.<sup>47</sup> Beside the vibrationless  $S_1$  state, several vibrational states of the first excited electronic level are clearly identified. These states are listed in Table 2. They were assigned by comparison to the experimental and calculated vibrational frequencies of the  $S_0$  state. Our assignment fits well that obtained by Balfour<sup>47</sup> from the high resolution spectrum of the  $S_1 \leftarrow S_0$  transition. There is only one discrepancy between ours and Balfour's assignment. By comparison of the corresponding frequencies in anisole and anisole<sup>+</sup> we assign the band at 427  $\text{cm}^{-1}$  to  $\nu_{16a}$  and not to an overtone as done by Balfour.

### 3.3. The excited state photoelectron spectra

Excited state photoelectron spectra of aromatic molecules have been reported in the literature for benzene,<sup>48</sup> toluene,<sup>49</sup>

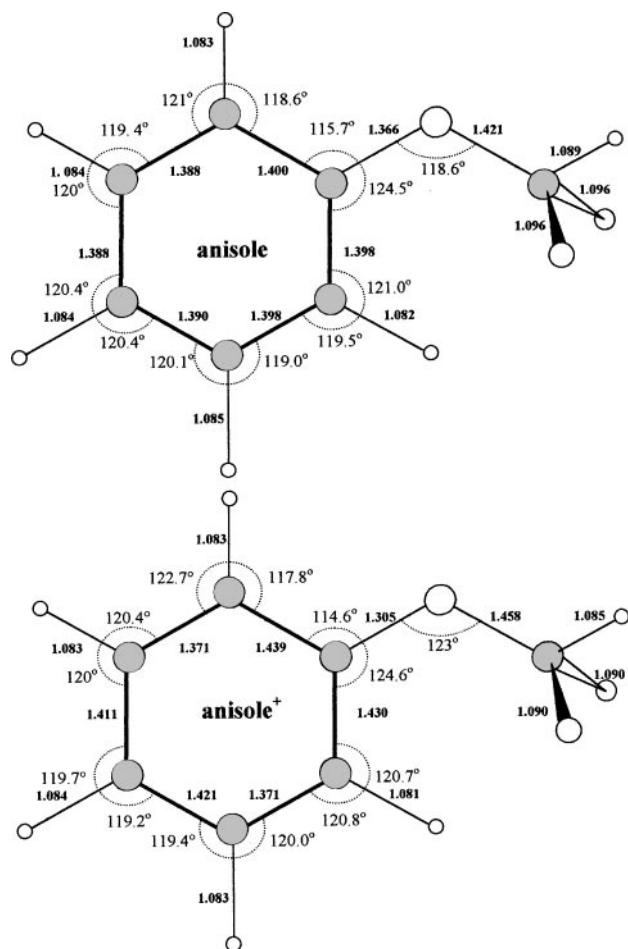


Fig. 2 Calculated *ab initio* structures of anisole and anisole cation. Bond lengths in Å and angles in degrees.

**Table 1** Assignment of the normal modes of anisole and of the anisole cation. The calculated values are scaled by a factor of 0.973 in the range 80–2000  $\text{cm}^{-1}$  and by a factor 0.963 in the range above 2000  $\text{cm}^{-1}$ . The experimental data given in column 1 are taken from the assignment given by Balfour.<sup>23</sup> Assignment marked with an asterisk are tentative

N	Sym.	Assignment	Anisole		Anisole cation	
			$\nu_{\text{exp}}/\text{cm}^{-1}$	$\nu_{\text{calc}}/\text{cm}^{-1}$	$\nu_{\text{exp}}/\text{cm}^{-1}$	$\nu_{\text{calc}}/\text{cm}^{-1}$
1	$a''$	COC torsion	81.5	90	110	114
2	$B_1$	$\nu_{10b}$ $\text{CH}_3$ torsion	209	203	165	147
3	$B_2$	$\nu_{9b}$ X sensitive	260	250	239	232
4	$a''$	O– $\text{CH}_3$ torsion	263	266	220	232
5	$A_2$	$\nu_{16a}$ CC twisting	415	412	365	367
6	$a'$	C–O–C bending	—	433	432	427
7	$B_1$	$\nu_{16b}$ C–C twisting	511	502	437	432
8	$A_1$	$\nu_{6a}$ X sensitive	553	543	540	532
9	$B_2$	$\nu_{6b}$ ring	618	610	568	560
10	$B_1$	$\nu_4$ X sensitive	690	669	616	603
11	$B_1$	$\nu_{11}$ C–H bending	752	738	771	763
12	$A_1$	C– $\text{OCH}_3$ stretch	788	777	727	762
13	$A_2$	$\nu_{10a}$ C–H bending	819	806	788	776
14	$B_1$	$\nu_{17b}$ C–H bending	880	867	925	919
15	$A_2$	$\nu_{17a}$ C–H bending	956	941	996	977
16	$B_1$	$\nu_5$ C–H bending	975	956	983	974
17	$A_1$	$\nu_{12}$ ring bending	997	981	978	971
18	$A_1$	$\nu_1$ ring breathing	1022	1015	983	973
19	$a'$	$\nu_{18a}$ O– $\text{CH}_3$ stretch.	1039	1041	946	937
20	$B_2$	$\nu_{18b}$ C–H bending	1073	1075	1077	1083
21	$a'$	$\text{CH}_3$ rocking	1143	1138	1107	1114
22	$B_2$	$\nu_{15}$ CH bending	1151	1147	1122	1137
23	$A_1$	$\nu_{9a}$ C–H bending	1169	1165	1175	1175
24	$a''$	$\text{CH}_3$ rocking	1180	1173	1139	1163
25	$A_1$	$\nu_{7a}$ C– $\text{OCH}_3$ stretch.	1253	1248	1328	1337
26	$B_2$	$\nu_3$ C–H bending	1292	1305	1301	1293
27	$B_2$	$\nu_{14}$ C–C stretching	1332	1330	1345	1360
28	$a'$	$\text{CH}_3$ sym. def.	1442	1437	1412	1414
29	$B_2$	$\nu_{19b}$ C–C stretch def	1455	1449	1491	1503
30	$a'$	$\text{CH}_3$ antisym. def.	1452	1456	1454	1455
31	$a''$	$\text{CH}_3$ antisym. def.	1464	1469	1435	1445
32	$A_1$	$\nu_{19a}$ C–C stretching	1497	1492	1473	1482
33	$B_2$	$\nu_{8b}$ C–C stretching	1588	1542	1482	1503
34	$A_1$	$\nu_{8a}$ C–C stretching	1599	1606	1574	1597
35	$A_1$	$\text{CH}_3$ sym. stretch.	2900	2903	2957	2960
36	$a''$	$\text{CH}_3$ asym. stretch.	2942	2964	3049	3052
37	$a'$	$\text{CH}_3$ asym. stretch.	3004	3034	3095*	3095
38	$A_1$	$\nu_{7b}$ C–H stretching	3026	3063	3098*	3096
39	$B_2$	$\nu_{13}$ C–H stretching	3037	3070	3103*	3103
40	$A_1$	$\nu_2$ C–H stretching	3062	3089	3105	3107
41	$B_2$	$\nu_{20b}$ C–H stretching	3092	3093	3113	3116
42	$A_1$	$\nu_{20a}$ C–H stretching	3105	3101	3121	3122

halogenated benzenes,<sup>50</sup> benzaldehyde<sup>51</sup> and naphthalene.<sup>24</sup> The structure of the spectra of these compounds has been discussed using a few specific normal modes which fit the most intense observed peaks. Using different intermediate states the

shape of the spectra changes considerably. In this section we report on the excited state photoelectron spectra of anisole, using the vibrationless state  $S_1$  and its vibrationally excited states  $\nu_{9b}$ ,  $\nu_{16a}$ ,  $\nu_{6a}$ ,  $\nu_{6b}$ , the C– $\text{OCH}_3$  stretch,  $\nu_{12}$  and  $\nu_1$  as

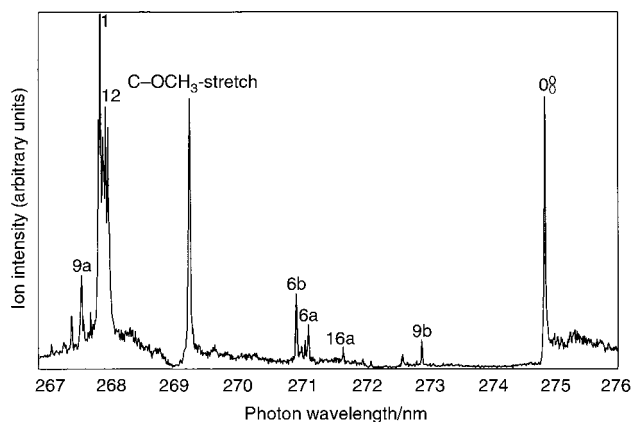


**Fig. 3** REMPI spectrum of anisole. The vibrational states labelled in the spectrum (except 9a) have been used as intermediate states for the excitation of the photoelectron spectra.

**Table 2** Vibrational frequencies<sup>a</sup> in the  $S_1$  state of anisole as obtained from the REMPI spectrum

0 ← 0	Symm.	$\nu(S_1)^b$	$\nu(S_1)^c$	$\nu(S_1)^d$	$\nu(S_0)^e$
9b	$B_2$	260	259	260	250
16a	$A_2$	427	—	415	412
6a	$A_1$	501	495	553	543
6b	$B_2$	526	526	618	610
C– $\text{OCH}_3$ stretch	$A_1$	756	759	788	777
12	$A_1$	942	938	997	981
1	$A_1$	950	953	1022	1015
9a	$A_1$	992	993	1169	1165
3	$B_2$	—	1127	1292	1305
14	$B_2$	—	1177	1332	1330
7a	$A_1$	—	1271	1253	1248
19a	$A_1$	—	1451	1497	1492
8b	$A_1$	—	1567	—	1542
13	$A_1$	—	3097	—	3101

<sup>a</sup> In  $\text{cm}^{-1}$ . <sup>b</sup> This work. <sup>c</sup> Ref. 47. <sup>d</sup> Ref. 35. <sup>e</sup> Calc.



intermediate states. The 2-photon absorption at the corresponding frequencies exceeds the ionization potential of anisole.

The resulting different photoelectron spectra, shown in Fig. 4, exhibit a characteristic coarse structure, depending upon the energy of the vibrationally excited state used in the different ionization pathways. In the “0–0” spectrum there are fourteen discernible peaks, but only the first six peaks from I to VI are labelled in Fig. 4.

If the spectra are plotted on an extended scale, as shown in Fig. 5, one recognizes a reproducible fine structure in the electron yield curve. At the origin the spectra are blurred to a few structural features, mainly inflections, but peaks become more and more pronounced on going to lower photoelectron energies.

**3.3.1. The “0 ← 0” photoelectron spectrum.** The molecular geometry of anisole in the  $S_1$  state has been recently determined from the rotational structure of a high resolution LIF spectrum of the  $S_1 \leftarrow S_0$  transition.<sup>27</sup> Anisole in the  $S_1$  state is still planar, as in the  $S_0$  state, but its geometry, as expected

from the lowering of the electron density in the ring, is an intermediate between that of anisole and of anisole<sup>+</sup>. In particular, the C–O–CH<sub>3</sub> angle is increased by 2.1 degrees with respect to neutral anisole. The four C–C bonds not parallel to the C–O bond are increased in length.

The photoelectron spectrum of Fig. 4(a), obtained *via* the vibrationless  $S_1$  state, will be now discussed below in some details. Four peaks (I, IV, V and VI) dominate the coarse structure. In the spectrum of anisole cation, as can be seen from Table 1, there is a strong accumulation of normal modes in five spectral regions, that can be arranged in five bunches of modes. It is therefore reasonable to expect that the population of these five bunches will be imaged in the coarse structure of the spectrum.

The most intense spectral feature is signal I. The signal intensity rises steeply from the onset at 8.232 eV to a maximum at 8.26 eV. The shape of the signal is very smooth and no structural features are recognizable except two inflections close to the maximum. The energy difference between the onset and the maximum of the signal correlates well with the  $\nu_{9b}$  mode of the cation. Obviously the propensity rule ( $\Delta v = 0$ ) is not valid in this case,  $\Delta v = 1$  being favored in the

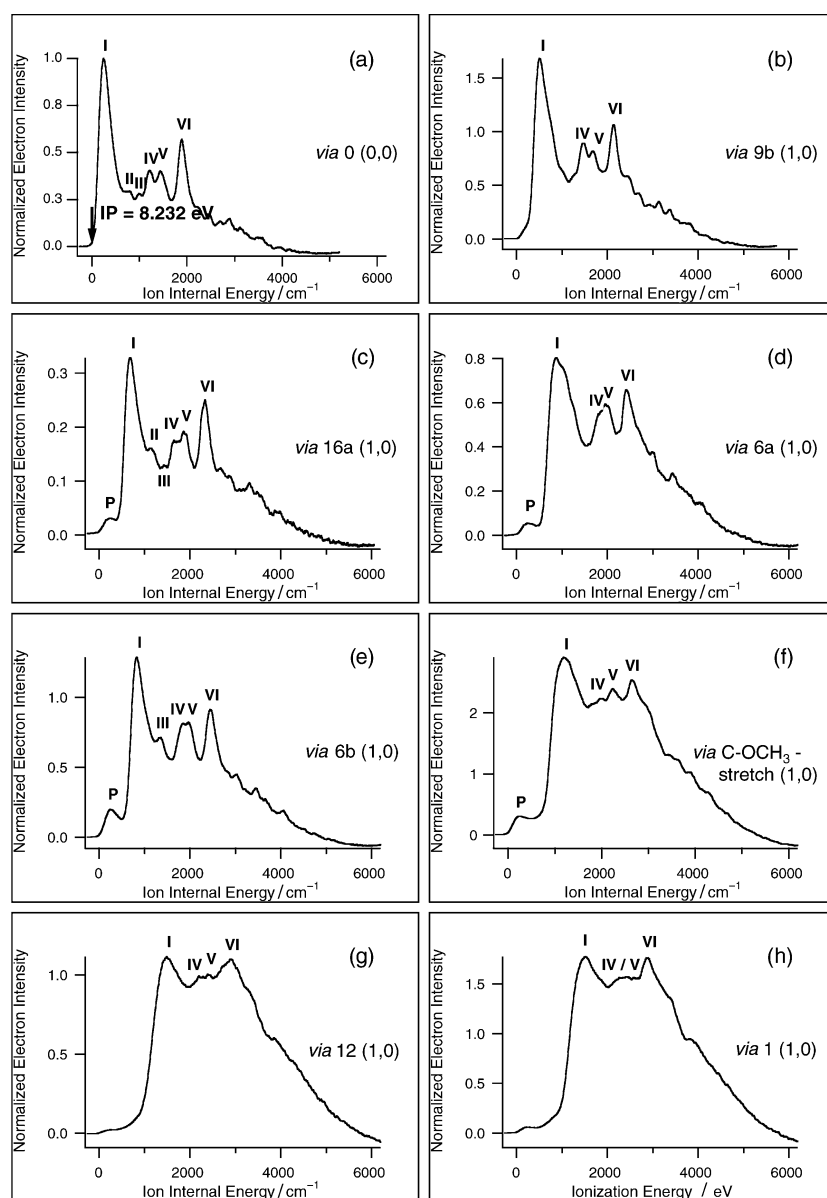


**Fig. 4** Photoelectron spectra of anisole *via* several vibrational levels in the  $S_1$  state. The arrow shows the adiabatic ionization potential. The range of the signals I–VI represents the low resolution part of the spectra. Above signal VI on an extended scale a rich and reproducible fine structure is observed. A detailed analysis of this fine structure will be published in a forthcoming paper.

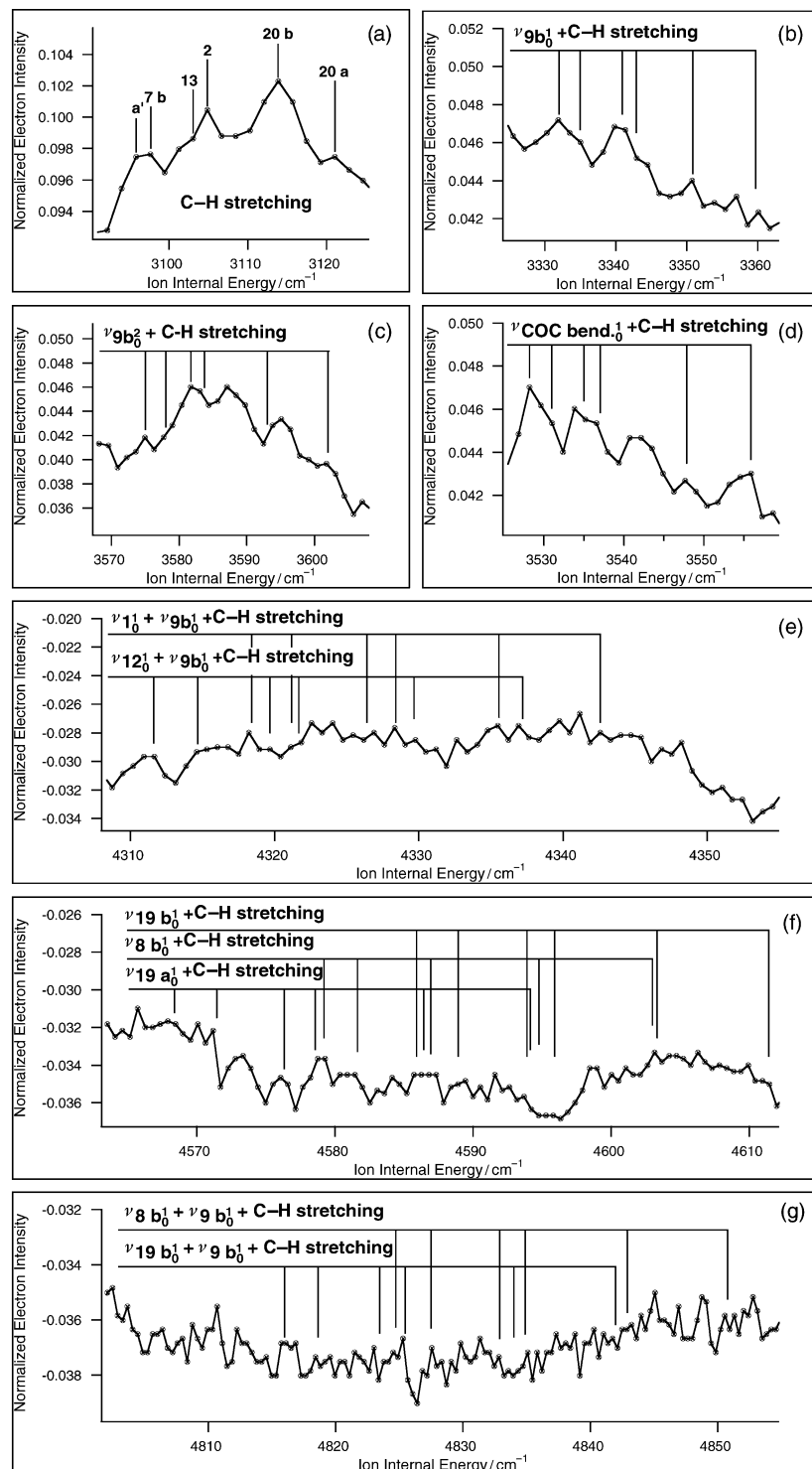


**Fig. 5** Assignment of the C–H stretching vibrations and of some combinations of the anisole cation as an example of the 0–0 photoelectron spectrum in the high resolution range.

ionization from the vibrationless state  $S_1$ . This and the high intensity observed is supported by the variation in the geometry of the  $S_1$  state which favors the excitation of the  $\nu_{9b}$  mode.

In previous papers<sup>49,50</sup> the maximum of the first strong signal in the  $0 \leftarrow 0$  spectrum was assigned to the ionization potential without comment. We assign the onset of the electron yield curve to the adiabatic ionization potential and the maximum of the first strong signal to the vertical ionization potential. The adiabatic ionization potential correlates to the vibrationless electronic ground state of the ion whereas the vertical ionization potential correlates with the vibrational

state of the ion reached in a vertical transition from the initial state according to the Franck–Condon principle. The main contribution to signal I arises from one single normal mode, but from the width of the peak, contributions of other normal modes and of their overtones or combinations are very likely to occur, as discussed below.

The three inflections close to the maximum are correlated with the O–CH<sub>3</sub> torsional mode and with combinations of the CH<sub>3</sub> torsional mode with the C–O–C and with the O–CH<sub>3</sub> torsional modes. All other fundamental modes of the cation falling in the range of peak I up to about 665 cm<sup>−1</sup> as well as other possible overtones and combinations are not discernible

in the spectrum. This includes the  $2\nu_{9b}$  mode around  $478\text{ cm}^{-1}$  which may have considerable intensity.

Signal II is weak and appears as a shoulder in the electronic yield curve. It reveals some structure on an extended scale representation. Using the frequencies of Table 1, the observed peaks are assigned to the normal modes C–OCH<sub>3</sub> stretching,  $\nu_{11}$  and  $\nu_{10a}$ . In addition, several symmetry allowed combinations fit well the observed peaks. Some of them are enhanced by superposition of different binary combinations. The contribution of the  $\nu_{9b}$  mode to these combinations is preferred due to the high population of this state. Combinations of  $\nu_{9b}$  with the in-plane C–O–C bending and with modes  $\nu_{6a}$  and  $\nu_{6b}$  are separately identified.

Signal III is also weak and smooth in shape. It shows inflections on the low energy side close to the maximum at  $989\text{ cm}^{-1}$  and two noticeable features at  $1007$  and  $1029\text{ cm}^{-1}$ . The normal modes  $\nu_{17b}$ ,  $\nu_{12}$ ,  $\nu_5$ ,  $\nu_1$  and  $\nu_{17a}$  and the O–CH<sub>3</sub> stretching mode contribute to peak III. The maximum is correlated with mode  $\nu_{17a}$ , whereas the other modes contribute to the low energy wing of the signal. Binary combinations are also expected in this range. A detailed inspection of the spectrum reveals the position of some of them. At the maximum of peak III the combinations of the O–CH<sub>3</sub> torsion with  $\nu_{11}$  and of the C–O–C bending mode with  $\nu_{6b}$  are superimposed on the  $\nu_{17a}$  mode. The signal observed at  $1007\text{ cm}^{-1}$  may be explained mainly by the combination of the C–O–C bending mode with  $\nu_{6b}$ . The second peak in this range at  $1029\text{ cm}^{-1}$  is assigned to the combinations  $\nu_{10a} + \text{CH}_3$  torsion, C–O–C torsion +  $\nu_{17b}$  and to some ternary combinations of  $\nu_{9b}$  with other modes like  $2\nu_{9b} + \nu_{6b}$  and  $\nu_{9b} + \text{CH}_3$  torsion +  $\nu_4$ . The low intensity of the signal points to low FC factors for the transition leading to these states. The normal mode  $\nu_3$  expected close to the minimum between peaks III and IV is hardly observable.

Signal IV is very smooth on its low energy side. Around the maximum at  $1212\text{ cm}^{-1}$  one finds structures at  $1192$  and  $1229\text{ cm}^{-1}$ . The low energy side is obviously dominated by the normal modes  $\nu_{18b}$ ,  $\nu_{15}$ ,  $\nu_{9a}$  and by the CH<sub>3</sub> rocking modes  $a'$  and  $a''$  which cannot be separated in the spectrum. The high energy side shows several steplike inflections. It is not meaningful to discuss all different combinations which may contribute to the signal. It is sufficient to point out that it gains most of its intensity from binary combinations of  $\nu_{9b}$  with  $\nu_5$ ,  $\nu_{12}$ ,  $\nu_1$  and  $\nu_{18a}$  and from ternary combinations of  $\nu_{9b}$  with other modes. Around the maximum the combinations  $\nu_{16b} + \nu_{10b}$ ,  $\nu_{16b} + \nu_{10a}$ , and the combinations of the C–O–C torsion mode with  $\nu_{17a}$  as well as with  $\nu_{17b}$ ,  $(\nu_{9b} + \nu_{18b})$ ,  $(\nu_{9b} + \nu_5)$  and  $(\nu_{9b} + \nu_{18a})$  are superimposed.

For signal V one finds a situation similar to that of signal IV. The signal appears smooth, but shows a significant number of inflections. The number of normal modes and combinations, in particular those including  $\nu_{9b}$  or the C–O–C in-plane bending mode is very high. The normal modes  $\nu_{7a}$  and  $\nu_{14}$  are expected in the onset region of this signal and are observed as inflections. The three deformation modes of the methyl group and the normal modes  $\nu_{19a}$ ,  $\nu_{19b}$ ,  $\nu_{8a}$  and  $\nu_{8b}$  give rise to clear inflections and signals around the maximum. The expected position of the antisymmetric CH<sub>3</sub> deformation mode coincides with the maximum of signal V at  $1436\text{ cm}^{-1}$ . The main contribution of combinations arises from coupling of  $\nu_{9b}$  with  $\nu_{9a}$ ,  $\nu_{7a}$ ,  $\nu_{15}$ ,  $\nu_{14}$ ,  $\nu_{19b}$  and with the CH<sub>3</sub> rocking mode. Combinations of the C–O–C in-plane bending mode as well as of  $\nu_{6a}$  and  $\nu_{6b}$  with  $\nu_{12}$ ,  $\nu_1$ ,  $\nu_{18b}$  and with the CH<sub>3</sub> rocking mode can be localized as inflections.

Signal VI covers the range  $1671$ – $2163\text{ cm}^{-1}$  above the onset. In this range no fundamental modes are expected and thus the signal is due only to the high density of combinations in this energy range. Again the symmetry allowed combinations of  $\nu_{9b}$  and of the C–O–C in-plane bending mode with other normal modes dominate, beside those of  $\nu_{6a}$  and

$\nu_{6b}$ . Actually, in the same frequency range several ternary combinations including  $\nu_{9b}$  and  $2\nu_{9b}$  may contribute significantly to the signal and prevent the appearance of a detectable fine structure.

At this point of the analysis we conclude that bunches of fundamental vibrations are not responsible for the strong signals observed in the spectrum. Fundamental modes contribute to the electron yield curve, but the coarse structure is strongly influenced by the manifold of binary and ternary combinations as convincingly demonstrated by the high intensity of signal VI.

In the following region above signal VI some small signals (VII–XIV) are observed and the electron yield curve seems to become more noisy. But the detailed inspection of this range reveals a rich and reproducible fine structure of the spectrum. From the analysis of this fine structure the coupling of normal modes to binary and ternary combinations can be observed. In this paper we present only some related examples demonstrating the development of fine structure with decreasing photoelectron energy. More details will be discussed in a forthcoming paper.

According to the assignment of the anisole cation modes (Table 1), most of the C–H stretching fundamentals occur between  $3095$  and  $3121\text{ cm}^{-1}$ . As shown in Fig. 5, combinations of these modes with one or two lower frequency modes lead to the fine structure of the spectrum.

Fig. 5(a) shows the  $0 \leftarrow 0$  spectrum in the narrow range  $3090$ – $3125\text{ cm}^{-1}$  with a point to point distance of about  $1.8\text{ cm}^{-1}$ . There are four signals which fit the positions calculated from the frequencies of Table 1. The six C–H stretching vibrations are not completely resolved, but can be easily identified.

Fig. 5(b) and (d) show the combinations of the same C–H stretching modes with  $\nu_{9b}$  and with the C–O–C in-plane bending mode. The signals are shifted in the spectrum by  $240$  and  $432\text{ cm}^{-1}$ , respectively. The spacing between the signals of the C–H stretching modes remains constant. There are some additional signals in this part of the spectrum which can be assigned to combinations of other fundamental modes.

Fig. 5(c) shows the spectral region where the combinations of the stretching modes with the overtone  $2\nu_{9b}$  are expected. One finds a reasonable agreement with the spectrum, although the superposition with the combinations  $\nu_1 + 2\nu_{19b}$ ,  $\nu_{12} + 2\nu_3$  and  $\nu_1 + 2\nu_3$  leads to a considerable modification of the signals.

Fig. 5(e)–(g) show the parts of the spectrum where the spacing between states becomes very narrow and their superposition leads to a complicated signal pattern. The point to point distance in these figures is about  $0.5\text{ cm}^{-1}$  and the signal to noise ratio in Fig. 5(g) is close to 5.

In the spectrum 5(e) one expects the combinations of normal mode  $\nu_{12}$  and  $\nu_1$  with the C–H stretching modes. The spectrum in this region is not well resolved but still one can recognize the expected sequences of combinations beside other signals. An analogous situation is encountered in Fig. 5(f). Most of the signal in this spectral region can be assigned to combinations of  $\nu_{19a}$ ,  $\nu_{19b}$  and  $\nu_{8b}$  with the aforementioned group of C–H modes. In Fig. 5(g) the ternary combinations of  $\nu_{9b}$  with  $\nu_{19a}$ ,  $\nu_{19b}$  and with the C–H stretching modes produce most of the signals.

The complete analysis of the fine structure of the spectrum shows that the calculated combination modes fit the structure of the experimental spectrum very well. This confirms our assignment presented in Table 1 for the cation.

### 3.3.2. Photoionization via different vibrational states of S<sub>1</sub>.

The excited state photoelectron spectra obtained using as resonant intermediate states of S<sub>1</sub> the normal modes  $\nu_{9b}$ ,  $\nu_{16a}$ ,  $\nu_{6a}$ ,  $\nu_{6b}$ , C–OCH<sub>3</sub> stretch,  $\nu_{12}$  and  $\nu_1$  are shown in Fig. 4(b)–(f). Table 3 summarizes the position of the maxima with respect to the onset in the different spectra. Only the coarse

**Table 3** Positions of the maxima I–VI in the photoelectron spectra (Fig. 4). The frequencies are given relative to the onset of the spectrum

Symm.	0 ← 0 —	9b B <sub>2</sub>	16a A <sub>2</sub>	6a A <sub>1</sub>	6b B <sub>2</sub>	C–OCH <sub>3</sub> str. A <sub>1</sub>	12 A <sub>1</sub>	1 A <sub>1</sub>
$\nu_1(S_1)$	—	260	427	501	526	756	942	950
Signal P	—	—	239	228	240	323	242	268
Signal I	241	481	697	882	823	1259	1522	1449
Signal II	792	—	1141	—	—	—	—	—
Signal III	990	—	1140	—	1359	—	—	—
Signal IV	1212	1461	1661	—	1820	2039	2208	2245
Signal V	1436	1648	1867	1950	2028	2319	2399	2440
Signal VI	1889	2125	2349	2421	2458	2735	2890	2931

structure of the spectra will be discussed here, using the signals I–VI of the 0 ← 0 spectrum as reference.

As shown in Fig. 4(a)–(f), the spectral pattern changes continuously. The strongest signals are shifted to higher energy. A small pre-signal P appears in the spectrum just before signal I. The position of the maximum of this signal remains constant at higher excitation energies, whereas the positions of the other signals are shifted. In the following we discuss the structure of these spectra and analyze the differences between them.

The intensity of the electron yield curve represents the population of vibrational states in the ion.

Generally, the population of fundamental modes is higher than that of combinations but the number of combinations strongly exceeds that of the fundamentals. The population probabilities and the position of the combination states are more influenced by the ionization pathways than the normal modes. By choosing a specific vibrational mode as a resonant intermediate state, the population of this mode and of its combinations with other modes is preferred after ionization. Therefore, with increasing energy of the resonant intermediate state, the position of the signals caused by the population of combination states is shifted to higher energies and the intensity of these signals changes.

**3.3.3. The “ $\nu_{9b}$ ” photoelectron spectrum.** Photoionization via the  $\nu_{9b}$  state of  $S_1$  is of special interest because of the electronic motion coupling with this vibration. The onset of the electron yield curve is, within error limits, identical to that obtained in the 0 ← 0 spectrum but the shape of the coarse spectral pattern changes both in position and intensity of the signals.

In comparison to the 0 ← 0 spectrum the strongest signal I in the  $\nu_{9b}$  spectrum is shifted by 240 cm<sup>−1</sup> to higher energy, the intensity and the width being increased. It shows a kink near the onset which correlates with the  $\nu_{9b}$  state of the ion. The maximum of the signal has to be assigned to the  $2\nu_{9b}$  state and at the position of the  $3\nu_{9b}$  state the electron yield curve has still a remarkable intensity. The position of the maxima confirms again that the  $\Delta\nu = 1$  transition is preferred upon ionization from the  $S_1$  state. The electron yield curve is very smooth except for some inflections in the high energy wing which can be tentatively assigned by using the frequencies of Table 1. The main contribution to the high intensity and to the width of signal I may be due to transitions to the  $2\nu_{9b}$  states and to other vibrational states. The positions of the C–O–C bending mode and of  $\nu_{16a}$ ,  $\nu_{6a}$ ,  $\nu_{6b}$  and  $\nu_4$  are expected to be close to the maximum. At the end of the high energy wing of signal I there is an accumulation of fundamental states ( $\nu_{17b}$ ,  $\nu_{18a}$ ,  $\nu_{12}$ ,  $\nu_5$ ,  $\nu_1$ ,  $\nu_{17a}$ ,  $\nu_{18b}$ , CH<sub>3</sub> rocking and  $\nu_{15}$ ) giving rise to inflections in the spectrum. The high intensity of the signal points also to considerable contribution of the transitions to binary and ternary combination states including preferentially  $\nu_{9b}$ ,  $2\nu_{9b}$  and probably  $3\nu_{9b}$ .

The weak signals II and III in the 0 ← 0 spectrum are completely integrated in the strong signal I and in signal IV.

Signals IV and V are shifted to higher energy and their intensity ratio is reversed in comparison to that of the 0 ← 0 spectrum.

The main reason for the enhanced intensity of signal IV is the accumulation of fundamental vibrational states on the low energy side (CH<sub>3</sub> rocking,  $\nu_{9a}$ ,  $\nu_3$ ,  $\nu_{7a}$ ,  $\nu_{14}$ ), close to the maximum (symm. CH<sub>3</sub> deformation a', asymm. CH<sub>3</sub> deformations a'' and  $\nu_{19a}$ ) and on the high energy side ( $\nu_{8b}$ ,  $\nu_{19b}$  and  $\nu_{8a}$ ) of the signal. In addition, the population of combination states including preferentially the  $\nu_{9b}$ ,  $2\nu_{9b}$  and the C–O–C bending modes is expected to contribute to this signal. The signal shape is very smooth.

The intensity and the fine structure of signal V has to be accounted for only in terms of combinations. At the signal maximum the states  $\nu_{9b} + \nu_{9a}$ ,  $\nu_{9b} + \text{CH}_3$  symm. deformation,  $\nu_{9b} + \text{C–O–C}$  bending +  $\nu_{12}$ ,  $\nu_{9b} + \text{C–O–C}$  bending +  $\nu_1$  are superimposed on other combinations including essentially  $\nu_{9b}$  and its overtones. Signal VI corresponds to signal VI in the 0 ← 0 spectrum, but the maximum is shifted to higher energies by 236 cm<sup>−1</sup> and the intensity is increased. The signal is very smooth, its intensity can be explained only by the superposition of several combination states. A detailed discussion of the long list of combination states expected in this energy range would be meaningless. It is sufficient to point out that near the maximum several combinations including  $\nu_{9b}$  and  $2\nu_{9b}$  are accumulated. The Frank–Condon factors for transitions into these states seem to be rather high. This can be easily understood considering that the atomic displacements in the  $\nu_{9b}$  vibration prepare the structural changes from the  $S_0$  to the  $S_1$  state.

**3.3.4. The “ $\nu_{16a}$ ” photoelectron spectrum.** At a first glance the coarse shape of this spectrum and the number of signals seem to be similar to those of the 0 ← 0 spectrum. A closer inspection reveals, however, very remarkable differences.

The intensity of all signals in the spectrum is reduced in comparison to the 0 ← 0 and to the  $\nu_{9b}$  spectrum. A small pre-signal P appears in front of the strongest signal I. The maximum of signal P is located at 240 cm<sup>−1</sup> above the onset and therefore we assigned it to the  $\nu_{9b}$  vibration of the ion. The low population of the state by ionization reflects a low FC factor. This is reasonable since the coupling of  $\nu_{16a}$  and  $\nu_{9b}$  is symmetry forbidden and because there is no support by the electronic motion in  $S_1$ .

The origin of the strong signal I coincides with the position of the  $\nu_{16a}$  state of the ion. The maximum, above the onset, correlates very well with the  $2\nu_{16a}$  ( $\Delta\nu = 1$ ) state of the ion. The width of signal I is only 300 cm<sup>−1</sup> and the shape is very smooth. This prevents a detailed analysis of the states which contribute to it. In the range of signal I one expects fundamental states in the frequency range between  $\nu_{16b}$  and  $\nu_{17a}$ . Especially the modes  $\nu_{11}$ ,  $\nu_{10a}$  and the C–OCH<sub>3</sub> stretching may contribute to the intensity close to the maximum. The high energy wing of the signal presumably contains combinations of  $2\nu_{16a}$  with fundamental modes. The contribution



of combination states including the  $\nu_{9b}$  mode to the intensity cannot be excluded but does not seem to be significant in this case.

Signal II is observed between 1050 and 1350  $\text{cm}^{-1}$ . It is weak but shows some remarkable structural features which can be clearly assigned to the vibrations  $\nu_{18b}$  and  $\nu_{14}$  of the ion. In addition a few combinations of  $2\nu_{16a}$  with other fundamentals can be correlated with details in the fine structure of the signal. The energy range of signal II in the  $\nu_{16a}$  spectrum covers nearly the range of signal IV in the  $0 \leftarrow 0$  spectrum in which also the contribution of fundamental modes dominates. This kind of signal is stable in position relative to the onset, in contrast to signals predominantly due to combination modes which migrate on the energy scale depending on the modes preferably populated in the different excitation pathways.

The very weak signal III is observed in the range 1410–1580  $\text{cm}^{-1}$  above the onset. As can be seen from Table 1, it consists of an accumulation of normal mode states. This is confirmed in detail by the considerable fine structure of the signal which allows the assignment of single states between the symmetric  $\text{CH}_3$  deformation and mode  $\nu_{8b}$ . This small signal becomes visible due to the shift of the combination states in the high energy wing of signal V in the  $0 \leftarrow 0$  spectrum to higher energy. States of combination modes hardly contribute to this signal.

The signals IV and V in the range 1580–2110  $\text{cm}^{-1}$  overlap each other. Their intensity is completely due to combination states. The main contribution is due to combinations of  $2\nu_{16a}$  with fundamental modes up to the symmetric  $\text{CH}_3$  deformation at 1412  $\text{cm}^{-1}$ .

Signal VI (2110–2600  $\text{cm}^{-1}$ ) is very intense and smooth in shape. The flat maximum extends from 2325 to 2345  $\text{cm}^{-1}$ . Close to the onset of the signal one expects combinations of  $2\nu_{16a}$  with other normal modes. Ternary combinations of the type  $2\nu_{16a} + \nu_i + \nu_j$  are accumulated in the range of this signal together with a manifold of other ternary combinations.

The shift of the maxima of signals I, IV, V and VI in the spectrum *vs.* the corresponding signals of the  $0 \leftarrow 0$  spectrum is of 447  $\text{cm}^{-1}$ . This value is the difference between the energy of the  $2\nu_{16a}$  and  $\nu_{9b}$  states in the ion. It indicates that the signal shift is dominated by the contribution of combination states.

**3.3.5. The “ $\nu_{6a}$ ” photoelectron spectrum.** The spectrum shows a sharp onset followed by a small pre-signal P. The maximum of this small signal coincides with the  $\nu_{9b}$  mode in the ion. In the energy range of the signal one expects fundamental modes up to  $\nu_{16a}$  and in fact inflections of the electron yield curve can be assigned to these modes.

The maximum of the strongest signal I in the spectrum is shifted of 882  $\text{cm}^{-1}$  from the onset. It is very smooth and only a few weak inflections are recognized in the high energy range. The signal width is significantly enhanced in comparison to the  $0 \leftarrow 0$  spectrum and covers 1100  $\text{cm}^{-1}$ . The relative intensity of the maximum is lower than in the  $\nu_{9b}$  spectrum and higher than in the  $\nu_{16a}$  spectrum. In the energy range of signal I one expects contributions from all normal modes between  $\nu_{6a}$  and  $\nu_{8b}$  plus contributions from a manifold of combination states. The analysis of the weak inflections observed in the high energy wing of the signal indicates that ternary combinations of the modes  $\nu_{9b}$ , C–O–C in-plane bending and  $2\nu_{16a}$  with two other normal modes give obviously important contributions to the signal intensity.

The signals II and III are not separated and signal IV may be recognized as a shoulder in the low energy wing of signal V.

Signal V is again very broad but has a considerable amount of fine structure, completely due to overtones and combinations. The main contributions originate from ternary

combinations including modes  $\nu_{9b}$ , the C–O–C in-plane bending,  $\nu_{6a}$ ,  $\nu_{6b}$  and the C–OCH<sub>3</sub> stretching mode.

The third prominent signal (VI) in this spectrum also results completely from combinations. The high density of states blurs the structure and only few weak inflections arise from the accumulation of different states.

The C–H stretching modes are expected in the decreasing part of the spectrum above 8.55 eV but their position cannot be clearly identified.

**3.3.6. The “ $\nu_{6b}$ ” photoelectron spectrum.** The spectrum shows again the characteristic small pre-signal mainly due to the  $\nu_{9b}$  mode.

The  $\nu_{6b}$  state of the ion is located at the onset of the first strong signal. The maximum of this signal, shifted by 823  $\text{cm}^{-1}$  *vs.* the onset of the electron yield curve, may be assigned to the combination  $\nu_{6b} + \nu_{9b}$ . A considerable contribution to this signal is expected from the fundamental modes between  $\nu_{6b}$  and  $\nu_{9b}$  as well as from combinations. Among these, those including  $\nu_{9b}$ , the C–O–C in-plane bending,  $\nu_{6a}$  and  $\nu_{6b}$  are preferred. Taking into account possible ternary combinations it can be understood that the shape of the signal is very smooth and that only minor inflections can be recognized.

Signal II is not observed. The neighbouring small signal III is mainly based on the states of normal vibrations between  $\nu_3$  and  $\nu_{8a}$ . The maximum of the signal correlates with mode  $\nu_{7a}$ . Some structural features in the electron yield curve fit combinations of  $\nu_{6b}$  with modes between the C–OCH<sub>3</sub> stretching and  $\nu_{9b}$ .

Going forward in the spectrum a signal with a double maximum IV and V is observed. This signal is completely due to combinations. Combinations of mode  $\nu_{6b}$  with the modes between  $\nu_{18b}$  and  $\nu_{8a}$  may be the most important contributions to the signals. However, there are more than 70 ternary combinations located in this energy range. Therefore it is not surprising that there are no structural features which can be explained by simple combinations.

A comparable situation is found in the next strong signal VI. It covers a broad range of more than 700  $\text{cm}^{-1}$  in which all combinations between  $\nu_{12} + \nu_{7a}$  up to  $\nu_{8a} + \nu_{14}$  and a series of ternary combinations of  $\nu_{9b}$ , of the C–O–C in-plane bending mode, of  $\nu_{6a}$  and of  $\nu_{6b}$  with two other normal modes are expected.

**3.3.7. The “C–OCH<sub>3</sub> stretching” photoelectron spectrum.** This spectrum again shows a pre-signal with its maximum at the position of the  $\nu_{9b}$  state of the ion.

The strongest signal I is shifted to higher energies and the position of the maximum may be assigned to the combination of the C–OCH<sub>3</sub> stretching +  $\nu_{6a}$ . Other combinations of the C–OCH<sub>3</sub> stretching mode with  $\nu_{9b}$ , with the C–O–C in-plane bending mode and with mode  $\nu_{6a}$  also contribute to this signal, although the main contribution to the high intensity arises from fundamental vibrations. At the low energy side of the signal one expects the fundamental modes C–OCH<sub>3</sub> stretching (727  $\text{cm}^{-1}$ ) and  $\nu_{9a}$  (1175  $\text{cm}^{-1}$ ). The shape of the electron yield curve in this energy range is very smooth so that the position of these vibrations cannot be located. The high energy wing of the signal exhibits clear inflections, many of them assigned to fundamentals between mode  $\nu_3$  (1301  $\text{cm}^{-1}$ ) and mode  $\nu_{8a}$  (1574  $\text{cm}^{-1}$ ). In addition there are overtones and combinations falling in this energy range. The superposition of states leads to the observed fine structure. Signals corresponding to the signals II and III of the  $0 \leftarrow 0$  spectrum are not observed.

The next coarse structures in the spectrum given by the maxima at 2039  $\text{cm}^{-1}$  (signal IV), 2319  $\text{cm}^{-1}$  (signal V) and 2795  $\text{cm}^{-1}$  (signal VI) are completely due to the accumulation of overtones and combinations. Beyond about 3000  $\text{cm}^{-1}$  the

spectrum shows a more pronounced fine structure but the C–H stretching modes are hardly identified in some weak inflections in the range 2950–3150  $\text{cm}^{-1}$ . It must be mentioned that beginning with this spectrum the fine structure is less pronounced even under improved resolution. This may be due to the increasing IVR which reduces the lifetime of the final states obtained after ionization.

**3.3.8. The  $\nu_{12}$  and the  $\nu_1$  spectra.** As can be seen from Fig. 4 the loss of coarse structure which begins with the C–OCH<sub>3</sub> stretching spectrum continues here. The coarse structure of the  $\nu_{12}$  and of the  $\nu_1$  spectra is very similar. This is very reasonable since the intermediate vibrational states are very close in energy and belong to the same symmetry species.

The  $\nu_{12}$  spectrum also shows the pre-signal due to the  $\nu_{9b}$  mode but it is now weaker and very flat.

Signal I is the most intense and is followed by a broad signal, in which the three maxima III, IV and V and the broad signal VI are identified. Behind this signal the intensity strongly decreases. In this range no distinct signals are observed but on an extended scale a fine structure is still observed. Like in the C–OCH<sub>3</sub> stretching and in the  $\nu_1$  spectra the structural features seem broader in energy. This effect again may be due to the increasing IVR as mentioned above.

The origins of the specific shape of the  $\nu_{12}$  and of the  $\nu_1$  spectra are very similar. All vibrational states of the ion between  $\nu_{6a}$  and  $\nu_{8a}$  contribute to the intensity of signal I. In addition there are several combinations in the range of signal I which blur the fine structure. Near the maximum of this signal the combinations of mode  $\nu_{12}$  and of mode  $\nu_1$  with modes  $\nu_{6a}$ ,  $\nu_{6b}$ , and with the overtone  $2\nu_{9b}$  are expected. A detailed inspection of the spectrum reveals that in the range between 800 and about 2900  $\text{cm}^{-1}$  binary and ternary combinations dominate. Among the ternary combinations obviously those of fundamental modes with the combinations  $\nu_{12} + \nu_{9b}$ ,  $\nu_{12} + \nu_{16a}$ ,  $\nu_{12} + \nu_{6b}$ ,  $\nu_{12} + \text{C–OCH}_3$  stretching and the overtone  $2\nu_{12}$  are the most important ones. The strong signal V in the  $\nu_{12}$  spectrum is due to the accumulation of this kind of vibrations.

The shape of the  $\nu_1$  spectrum develops according to the same principles outlined for the  $\nu_{12}$  spectrum, *i.e.* the ternary combinations become more important for the general appearance of the spectrum mode  $\nu_1$  taking the role of mode  $\nu_{12}$ . There are only minor changes in the fine structure of the  $\nu_1$  in comparison to the  $\nu_{12}$  spectrum. They result from the different population of modes  $\nu_{12}$  and  $\nu_1$  in the  $S_1$  state as can be seen from the REMPI spectrum.

## 4. Conclusion

In this paper we report on the REMPI spectrum and the photoelectron spectra of anisole. The interpretation of the spectra has been made on the basis of *ab initio* calculations in the framework of the density functional theory. The *ab initio* calculated frequencies of the 42 normal modes of neutral anisole are in very good agreement with the experimental values reported by Balfour.<sup>23</sup> The calculated normal mode frequencies of the cation are confirmed by the experimental values obtained from the “0–0” photoelectron spectrum. The calculated variation of the geometry of the anisole cation with respect to that of neutral anisole is supported by high resolution investigations of the  $S_1$ – $S_0$  transition. The neutral and the ionic molecule are both planar but the C–O–C angle in the cation is increased by almost 4 degrees in comparison to neutral anisole.

The REMPI spectrum reveals several vibrations in the  $S_1$  state. The frequencies obtained for these vibrations are in excellent agreement with the data reported by Balfour. Several excited state photoelectron spectra have been measured. The

coarse structure of these spectra is characterized by a series of prominent signals depending on the energy of the  $S_1$  state vibration used as an intermediate state in the 2-photon ionization. The observed position and intensity of these signals changes considerably on going from the “0–0” to the “ $\nu_1$ ” spectrum. With increasing excitation energy the signals are shifted to higher energies, except for a small pre-signal the position of which remains unchanged. The population of vibrational states in the ion obviously depends on the vibration in the intermediate state  $S_1$  and therefore the ionization pathway influences the spectral pattern.

The selected population of vibrational states and their combinations is clearly detected in comparing the “0–0” spectrum to the “ $\nu_{9b}$ ” and the “ $\nu_{16a}$ ” spectra, where the  $\nu_{9b}$ , the  $2\nu_{9b}$  and the  $2\nu_{16a}$  states and their combinations are preferred. In addition, the geometry change in the  $S_1$  state supports the population of the  $\nu_{9b}$  and of the C–O–C in-plane bending modes in the ion. In this way the positions of highly populated levels are continuously shifted to higher energies.

The normal modes as well as the combinations contribute to the intensity of the signals. The position of the final states is not influenced by the different excitation pathway but their population changes. Owing to the large number of binary and ternary combinations, their contribution to the intensity of the signals obviously exceeds that of the normal modes. Therefore, the observed shift of the prominent signals in the different photoelectron spectra results from changes in the population of selected combinations.

Besides the coarse structure at lower photoelectron energies a pronounced fine structure is observed, mainly due to binary and ternary combinations of the C–H stretching modes with other normal modes. The analysis confirms the results of the *ab initio* calculations.

## Acknowledgement

One of us (S.C.) expresses his deepest thanks to the Alexander von Humboldt Stiftung for the award that has offered him the possibility of working in Germany. This research was supported by the E.C. (contract No HPRI-CT-1999-00111), by the Deutsche Forschungsgemeinschaft, the Fonds der Chemischen Industrie and by the Italian MURST.

## References

- 1 M. Schütz, T. Bürgi and S. Leutwyler, *J. Chem. Phys.*, 1993, **98**, 3763.
- 2 T. Ebata, M. Furukawa, T. Suzuki and M. Ito, *J. Opt. Soc. Am.*, 1990, **87**, 1890.
- 3 G. Hartland, B. Henson, V. Ventura and P. M. Felker, *J. Phys. Chem.*, 1992, **96**, 1164.
- 4 S. Tanabe, T. Ebata, M. Fujii and N. Mikami, *Chem. Phys. Lett.*, 1993, **215**, 347.
- 5 H. Abe, N. Mikami and M. Ito, *J. Phys. Chem.*, 1982, **86**, 1768.
- 6 A. Oikawa, H. Abe, N. Mikami and M. Ito, *J. Phys. Chem.*, 1983, **87**, 5083.
- 7 K. Fuke and K. Kaya, *Chem. Phys. Lett.*, 1983, **94**, 97.
- 8 R. J. Stanley and A. W. Castleman, Jr., *J. Chem. Phys.*, 1991, **94**, 7744.
- 9 R. J. Lipert and S. D. Colson, *J. Chem. Phys.*, 1988, **89**, 4579.
- 10 K. Wolf, H. H. Kuge, M. Schmitt and K. Kleinermauns, *Ber. Bunsen-Ges. Phys. Chem.*, 1992, **96**, 1309.
- 11 M. Pohl, M. Schmitt and K. Kleinermauns, *J. Chem. Phys.*, 1991, **94**, 1717.
- 12 R. J. Lipert and S. D. Colson, *Chem. Phys. Lett.*, 1989, **161**, 303.
- 13 M. Schmitt, H. Müller and K. Kleinermauns, *Chem. Phys. Lett.*, 1994, **218**, 246.
- 14 A. Sun and P. M. Johnson, *J. Chem. Phys.*, 1986, **84**, 1206.
- 15 (a) R. J. Lipert and S. D. Colson, *J. Phys. Chem.*, 1989, **93**, 195; R. J. Lipert and S. D. Colson, *J. Phys. Chem.*, 1990, **94**, 2358; (b) K. Kimura, *Adv. Chem. Phys.*, 1985, **60**, 161.
- 16 R. J. Lipert, G. Bermudez and S. D. Colson, *J. Phys. Chem.*, 1988, **92**, 3801.

- 17 A. Goto, M. Fujii, N. Mikami and M. Ito, *J. Phys. Chem.*, 1986, **90**, 2370.
- 18 G. Reiser, O. Dopfer, R. Lindner, G. Henri, K. Müller-Dethlefs, E. W. Schlag and S. D. Colson, *Chem. Phys. Lett.*, 1991, **181**, 1.
- 19 O. Dopfer, G. Reiser, K. Müller-Dethlefs, E. W. Schlag and S. D. Colson, *J. Chem. Phys.*, 1994, **101**, 974.
- 20 (a) S. L. Anderson, L. Goodman, K. Krogh-Jespersen, A. Ozkabak, R. Zare and C. Zheng, *J. Chem. Phys.*, 1985, **82**, 5329; (b) O. Dopfer and K. Müller-Dethlefs, *J. Chem. Phys.*, 1994, **101**, 8508.
- 21 P. Hobza, R. Burce, V. Spirko, O. Dopfer, K. Müller-Dethlefs and E. W. Schlag, *J. Chem. Phys.*, 1994, **101**, 990.
- 22 (a) G. Berden, W. L. Meerts, M. Schmitt and K. Kleinermanns, *J. Chem. Phys.*, 1996, **104**, 972; (b) S. Schumm, M. Gerhards and K. Kleinermanns, *J. Phys. Chem. A*, 2000, **104**, 10648; (c) H. D. Barth, K. Buckhold, S. Djafour, B. Reimann, K. Lommatzsch and B. Brutschy, *Chem. Phys.*, 1998, **239**, 49.
- 23 W. J. Balfour, *Spectrochim. Acta, Part A*, 1983, **39**, 795.
- 24 G. M. Anderson, P. A. Kollman, L. N. Domelsmith and K. N. Houk, *J. Am. Chem. Soc.*, 1979, **101**, 2344; H. Kenschin, H. Tilly and C. Grundfelt-Forsius, *J. Mol. Struct.*, 1981, **77**, 51.
- 25 M. Rumi and G. Zerbi, *J. Mol. Struct. (THEOCHEM)*, 1999, **509**, 11.
- 26 S. Tsuzuki, H. Houjou, Y. Najawa and K. Hiratani, *J. Phys. Chem. A*, 2000, **104**, 1332.
- 27 C. G. Eisenhardt, G. Pietraperzia and M. Becucci, *Phys. Chem. Chem. Phys.*, 2001, **3**, 1407.
- 28 A. D. Barker, D. P. May and D. W. Turner, *J. Chem. Soc. B*, 1968, 22; J. P. Maier and D. W. Turner, *J. Chem. Soc., Faraday Trans. 2*, 1973, **69**, 521; L. Klasinc, B. Kovac and H. Güsten, *Pure Appl. Chem.*, 1983, **55**, 289.
- 29 C. G. Eisenhardt and H. Baumgärtel, *Ber. Bunsen-Ges. Phys. Chem.*, 1998, **102**, 1803.
- 30 C. G. Eisenhardt, M. Oppel and H. Baumgärtel, *J. Electron Spectrosc. Relat. Phenom.*, 2000, **108**, 141.
- 31 P. Kruit and F. H. Read, *J. Phys. E*, 1983, **16**, 313.
- 32 O. Chesnovsky, S. H. Yang, C. L. Pettiette, M. J. Craycraft and R. E. Smalley, *Rev. Sci. Instrum.*, 1987, **58**, 2131.
- 33 G. Sanzone, *Rev. Sci. Instrum.*, 1970, **41**, 741.
- 34 P. Schwartze, H. Baumgärtel and C. G. Eisenhardt, *Rev. Sci. Instrum.*, 2001, **72**, 3125.
- 35 K. Tsutsumi, S. Sato and K. Kimura, personal communication, 1999.
- 36 R. G. Parr and W. Yang, *Density-Functional Theory of Atoms and Molecules*, Oxford University Press, Oxford, 1989.
- 37 M. J. Frisch *et al.*, *GAUSSIAN 98, Revision A.5*, Gaussian Inc., Pittsburgh, PA, 1998.
- 38 G. Rauhut and P. Pulay, *J. Phys. Chem.*, 1995, **99**, 3093.
- 39 A. P. Scott and L. Radom, *J. Phys. Chem.*, 1996, **100**, 16502.
- 40 P. C. Hariharan and J. A. Pople, *Theor. Chim. Acta*, 1973, **28**, 213.
- 41 A. D. Becke, *Phys. Rev. A*, 1988, **33**, 3098.
- 42 C. Lee, W. Yang and R. G. Parr, *Phys. Rev. B*, 1988, **37**, 785.
- 43 S. J. Vosko, L. Wilk and M. Nusair, *Can. J. Phys.*, 1980, **58**, 1200.
- 44 N. L. Owen and R. E. Hester, *Spectrochim. Acta, Part A*, 1969, **25**, 343.
- 45 H. C. Longuet-Higgins, *Mol. Phys.*, 1963, **6**, 445.
- 46 E. B. Wilson, Jr., *Phys. Rev.*, 1934, **45**, 706.
- 47 W. J. Balfour, *J. Mol. Spectrosc.*, 1985, **109**, 60.
- 48 Y. Achiba, K. Sato, K. Shobatake and K. Kimura, *J. Chem. Phys.*, 1983, **79**, 5213; Y. Achiba, A. Hiraya and K. Kimura, *J. Chem. Phys.*, 1984, **80**, 6047.
- 49 J. T. Meek, S. R. Long and J. P. Reilly, *J. Phys. Chem.*, 1982, **86**, 2809.
- 50 S. L. Anderson, D. M. Reder and R. N. Zare, *Chem. Phys. Lett.*, 1982, **93**, 11.
- 51 S. R. Long, J. T. Meek, P. J. Harrington and J. P. Reilly, *J. Chem. Phys.*, 1983, **78**, 3341.